# Improved energy spread in the radiation pressure acceleration of protons with a linearly polarized laser

B. S. Paradkar*

*UM-DAE Centre for Excellence in Basic Sciences, University of Mumbai, Mumbai 400098, India*

(Received 28 November 2022; revised 4 June 2023; accepted 14 July 2023; published 9 August 2023)

Degradation in the energy spread of accelerated protons due to the transverse instability induced transparency is one of the critical issues in the laser-driven radiation pressure acceleration (RPA) scheme. This issue is more severe for linearly polarized lasers due to enhanced heating of electrons. Therefore, in spite of being experimentally challenging, most of the numerical studies are performed with circularly polarized lasers. In this work, through particle-in-cell simulations, we demonstrate a significant improvement in the energy spread of the accelerated protons when a multilayered target is irradiated by a linearly polarized laser. This multilayered target consists of a near-critical-density (NCD) layer, sandwiched between a thick metallic foil and a thin RPA target. The role of the NCD target is to suppress the laser transparency to increase the coupling of laser momentum to the RPA protons. On the other hand, the metallic foil utilizes the kinetic energy of the escaping fast electrons to form an electrostatic sheath to filter the low-energy RPA protons. This results in significant improvement in the accelerated proton spectrum, even with a linearly polarized laser.

DOI: 10.1103/PhysRevE.108.025203

## I. INTRODUCTION

Laser-driven ion acceleration [1] is seen as the potential alternative to conventional ion beam radiation therapy. Although the idea of using the accelerated proton and carbon ion beams for the treatment of cancer was suggested more than 60 years ago [2], the technology based on conventional accelerators has still not found widespread success. Due to large acceleration lengths associated with such accelerators, only a limited number of hospitals have managed to build such hadron therapy facilities. Most of these facilities are in the developed world, and for the rest of the world, such a treatment is practically out of reach. Therefore, for making such a treatment more accessible across the globe, it is imperative to look for alternate acceleration schemes that can potentially be used in mid- and small-size hospitals.

The laser-driven ion accelerators, due to their compactness, can potentially replace the conventional accelerators for the use of hadron therapy at a much lower cost [3,4]. The two main mechanisms of laser-driven ion acceleration are target normal sheath acceleration (TNSA) [5] and radiation pressure acceleration (RPA) [6,7]. Acceleration through TNSA requires relatively lesser intensity of laser ($10^{18}$–$10^{20}$ W/cm$^2$) and thicker targets (mm size), whereas RPA can only be achieved at intensities above $10^{20}$ W/cm$^2$ with thinner targets of thickness 10–100 nm. Although TNSA is extensively studied due to its easier experimental accessibility, the number of experiments in the RPA regime have also increased in the last decade or so due to improvement in the laser intensities and target manufacturing techniques. The distinct advantage of RPA over TNSA is its higher conversion efficiency, whereas TNSA seems to be more robust in terms of stability of acceleration and shot-to-shot variation. It is envisaged that with more experimental investigation, RPA will be able to overcome this limitation and can seriously be considered for producing next-generation compact ion accelerators for hadron therapy.

One of the critical issues in the RPA scheme is degradation in the energy spectrum of the accelerated beam due to the growth of Rayleigh-Taylor-like transverse instability [8,9]. Although the physical origin of this instability is still debated [10–12], particle-in-cell (PIC) simulations have clearly demonstrated that the enhanced electron heating during the laser transparency phase of this instability is responsible for the degradation of the ion spectrum. To avoid electron heating, most PIC simulations are performed with circularly polarized lasers [13,14], whereas experiments are almost always carried out with linearly polarized lasers due to technological limitations. In this work, we address this issue by exploring the possibility of generating a quasimonoenergetic proton beam using a linearly polarized laser.

Using two-dimensional PIC simulations, we demonstrate a significant improvement in the energy spread of the accelerated proton beam when a linearly polarized laser is incident on a thin RPA target. The improvement is achieved through a different target design where a near-critical-density (NCD) target (such as foam targets) is sandwiched between a thin accelerating RPA foil and a thick metallic foil, as shown in Fig. 1. Our recent study [15] has shown that the suppression of laser transparency can be achieved by placing a NCD layer behind the RPA target. Such a target provides a return current of electrons to balance the escaping hot electrons from the RPA target. This restricts the depletion of electron density from the RPA target, leading to suppression of laser transparency and improvement in the coupling efficiency from the laser to the directed RPA ions. The role of the metallic foil placed

*bhooshan.paradkar@cbs.ac.in

 

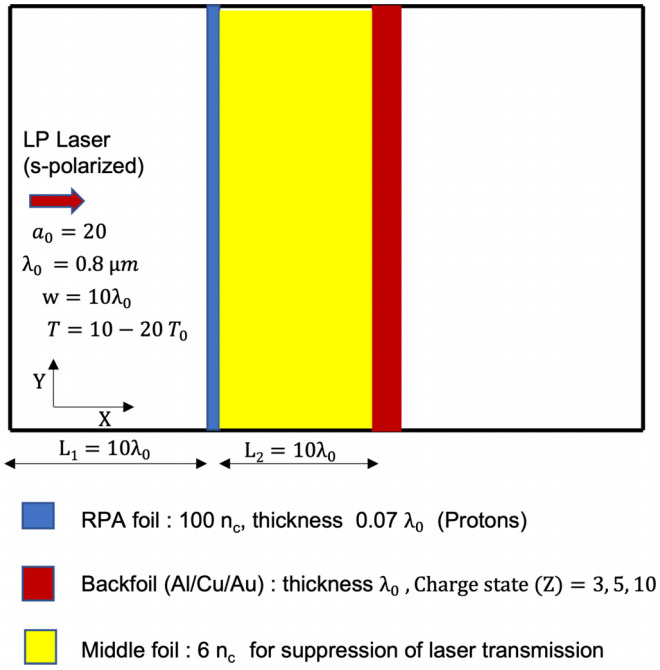


FIG. 1. Schematic of simulation setup. A linearly polarized laser is incident on a RPA foil. A near-critical-density ($6n_c$) target is kept in between the RPA target and a metallic foil (aluminum, copper, gold) with varying charge states. Three charge states ($Z = 3, 5, 10$) are considered for each metallic foil to investigate the role of the charge to mass ratio of ions on the electrostatic sheath formed around the metallic foil.

behind the near-critical-density target is to utilize the energy of escaping fast electrons in setting up a localized electrostatic potential well around it, similar to the TNSA mechanism. The RPA accelerated ions while crossing this potential well get filtered according to their incoming energy. While the low-energy ions which cannot overcome the potential barrier get reflected from the metallic foil, the sufficiently high-energy ions get an extra boost of energy while going downhill in the potential well. This process significantly improves the quality of the accelerated beam coming out of this. different target. Since the filtering process depends upon the strength of the electrostatic field around the metallic foil, we find that the charge state of the foil plays an important role. The potential well associated with very high charge states of the metallic foil tends to reflect all the RPA ions. Such high charge states can easily be achieved due to the direct interaction of intense laser with the metallic foil through optical field ionization. Therefore, the sandwiched near-critical-density target also plays an additional role of shielding the metallic foil from direct interaction with the laser to restrict the maximum charge states. The details of the numerical simulations along with the physics of the above-mentioned results will be discussed in the paper.

The paper is organized as follows: The details of the numerical setup of the simulations are given in Sec. II. The results of the numerical simulations are described in Sec. III, which is followed by Sec. IV, which gives a detailed physics discussion of the results. Finally, in Sec. V, we summarize our results and give the concluding remarks.

## II. NUMERICAL SETUP

Numerical simulations are carried out with an indigenously developed two-dimensional PIC code, AGASTHII-py [15]. The setup of the simulation is shown in Fig. 1 where a multilayered target, having a thin RPA foil (blue color) at the front, is irradiated by a linearly ($s$-polarized) polarized laser of normalized vector potential $a_0 = 20$ and wavelength $\lambda_0 = 800$ nm. The corresponding intensity is about $8 \times 10^{20}$ W/cm$^2$. The spot-size and pulse duration of the laser are taken as $10\lambda_0$ and $10T_0$, respectively, where $T_0$ is the time period. Such laser parameters are well within the reach of present-day laser technology. We have also carried out a few test simulations with a $p$-polarized laser to ensure that spatial anisotropy arising in realistic three-dimensional simulations does not affect the physics discussed in this paper. The simulations are carried out with uniform spatial resolution of $\lambda_0/120 \times \lambda_0/12$ in the longitudinal ($X$) and transverse ($Y$) directions, respectively. Numerical convergence of the results is checked by doubling the resolution for a few simulations. In the RPA target, 100 macroparticles per cell are used, whereas other targets are simulated with 4 particles per cell.

A RPA target having proton density $n = 100n_c$ and thickness $0.07\lambda_0$ (shown in blue) is kept at $10\lambda_0$ from the left simulation boundary. The thickness of the RPA target is chosen from optimum thickness considerations ($l_{opt}/\lambda_0 \simeq a_0 n_c/\pi n_0$) based on the one-dimensional light-sail model [7]. A near-critical-density (NCD) target (shown in yellow) of thickness $10\lambda_0$ and density $6n_c$ is kept behind the RPA foil, whereas a metallic foil of thickness $\lambda_0$ (shown in red) is placed at the back of the NCD target. We have considered three options for the metallic foil, viz., aluminum (Al), copper (Cu), and gold (Au). The number density of ions ($n_i$) in the metallic foil is taken according to the mass density of the foil, whereas the corresponding electron density is chosen as $n_e = Zn_i$, where $Z$ is the charge state of the metallic foil. Three charge states ($Z = 3, 5, 10$) of metallic foil are considered. Such ionization states can either be produced through self-consistent interaction of expanding hot plasma with the metallic foil or through the initial interaction of a low-intensity laser irradiated from the rear side of the target. Ideally, detailed ionization physics must be included for the self-consistent modeling of such metallic foils. However, for simplicity in the present studies, we consider the charge state of the foil as one of the input parameters to investigate its role on accelerated proton energies.

Since the role of metallic foil is to set up a TNSA-like electrostatic potential, by varying the charge states ($Z$) and ion mass ($M$), we intend to investigate the sheath physics in detail. Typically, higher charge states should lead to stronger sheath potential, which will impact the filtering process of low-energy RPA protons. On the other hand, ion mobility is important in sustaining the sheath potential. Once the ions in the metallic foil become mobile, the sheath potential should drop, which can eventually alter the response of the RPA protons. Thus, by changing the charge state along with the material (Al, Cu, Au), we investigate the role of the charge to mass ratio of ions ($Z/M$) on the quality of the accelerated RPA beam coming out from the rear side of the target. We also carry out simulations with RPA + metallic foil (without the NCD layer) and RPA + NCD layer (without the metallic

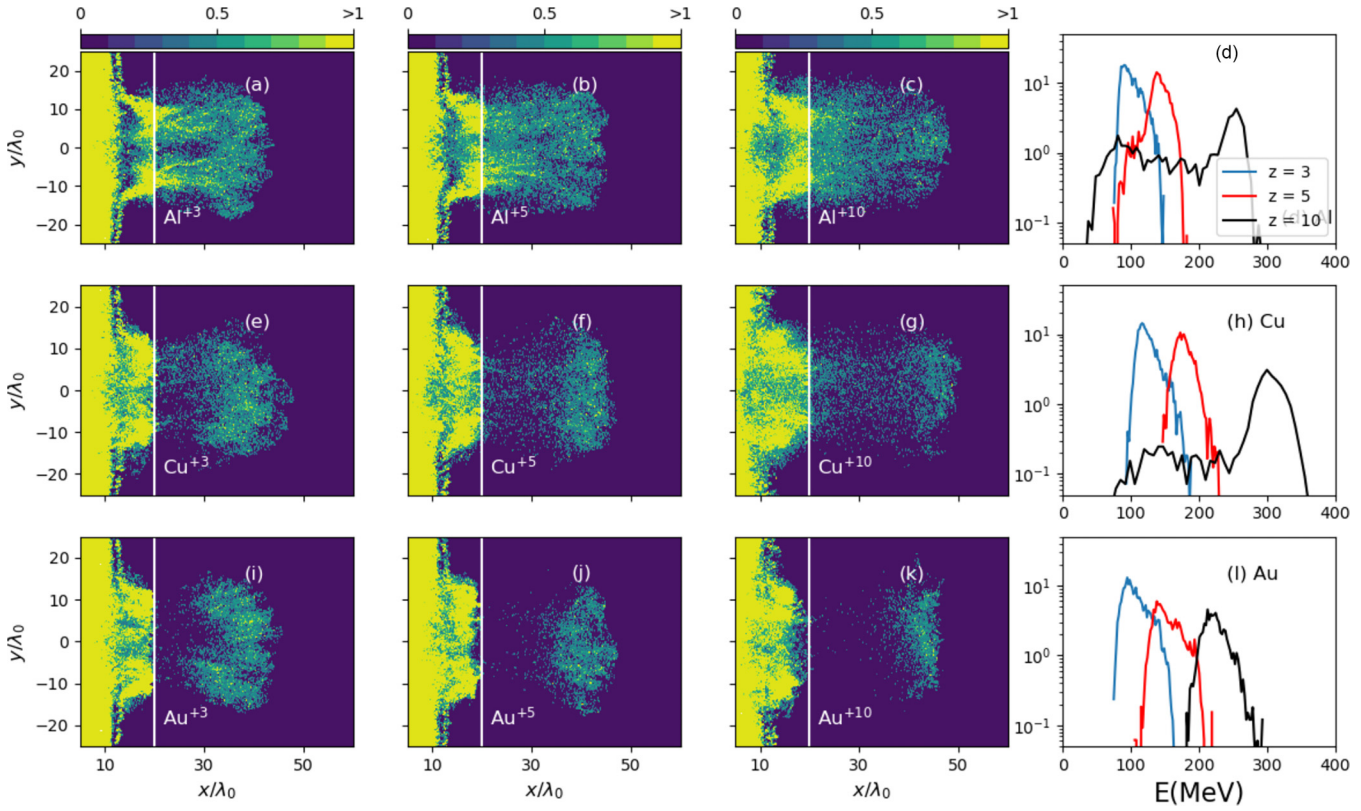


FIG. 2. Simulation results ($\omega_0 t = 742$) with a multilayered target shown in Fig. 1: Initial locations of the RPA foil and metallic foil (white line) are $X = 10\lambda_0$ and $X = 20\lambda_0$, respectively. The normalized proton densities (from RPA foil) are shown for (a)–(c) aluminum, (e)–(g) copper, and (i)–(k) gold backfoils for various charge states ($Z = 3, 5, 10$). Associated spectra of the accelerated protons are shown in (d), (h), and (l).

foil) to investigate the explicit role of the metal foil and NCD layer in the dynamics of RPA proton acceleration.

## III. RESULTS

In this section, we first discuss the simulations with a multilayered target, described in Fig. 1. The summary of the results at time $\omega_0 t = 742$ in shown in Fig. 2. At this time, interaction of the laser with the RPA target is over. Therefore, the proton energies reported in the paper give an upper bound for the laser parameters used in the simulations. All results reported in the paper correspond to the same time. Figures 2(a)–2(c) show the density of RPA protons when an aluminum metal foil ($Al^{+3}$, $Al^{+5}$, $Al^{+10}$) is placed at the back of the near-critical-density target. The corresponding accelerated proton spectra are shown in Fig. 2(d). Similar plots for copper and gold foils are shown in Figs. 2(e)–2(h) and Figs. 2(i)–2(l), respectively. The white vertical line ($x = 20\lambda_0$) in the density contour plots represents the initial location of the metallic foil. Since we are mainly interested in the forward moving proton beam, only the macroparticles with $x > 30\lambda_0$, i.e., at least $10\lambda_0$ away from the metallic foil, are considered while calculating the accelerated RPA proton spectra. The energy spread is characterized from the root-mean-square (rms) of the energies of these accelerated protons. The charge (per unit length) and energy of these protons is given in Table I. Here, charge per unit length is reported since simulations are carried out in a two-dimensional (2D) Cartesian geometry.

From Table I, we observe that with increasing charge states ($Z$), the proton beam gains more energy but at the cost of loss of particles. For example, as the charge state of the aluminum target increases from 3 to 10, the mean energy of the accelerated beam increases from 101.4 to 183.3 MeV, but the charge per unit length reduces from 513.7 to 270.4 pC/μm. The reduction in accelerated charge with increasing $Z$ is also evident from the RPA proton density contours given by Fig. 2. The energy spread in almost all cases is found to be around 10–20% with an exception of aluminum foil with $Z = 10$. The

TABLE I. Charge (pC/μm) and energy (MeV) of accelerated protons for different backfoils shown in Fig. 2. Note that protons with $x > 30\lambda_0$ are considered for these calculations.

| Backfoil material | Charge state ($Z$) | $Q$ (pC/μm) | $E$ (MeV) |
|---|---|---|---|
| Al | 3 | 513.7 | $101.4 \pm 14.0$ |
| Al | 5 | 404.5 | $139.7 \pm 16.3$ |
| Al | 10 | 270.4 | $183.3 \pm 72.4$ |
| Cu | 3 | 405.3 | $125.9 \pm 15.5$ |
| Cu | 5 | 292.2 | $177.9 \pm 13.3$ |
| Cu | 10 | 160.1 | $281.3 \pm 59.0$ |
| Au | 3 | 416.1 | $107.5 \pm 17.7$ |
| Au | 5 | 214.1 | $154.2 \pm 19.4$ |
| Au | 10 | 154.1 | $224.0 \pm 17.8$ |

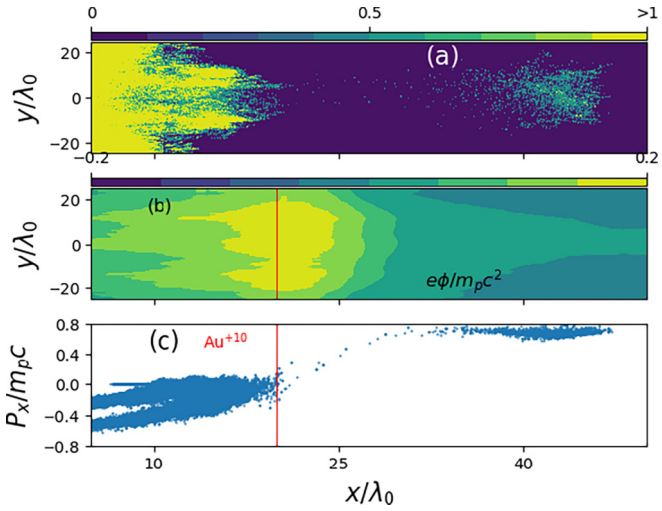


FIG. 3. Summary of simulations ($\omega_0 t = 742$) with middle foil (case II of Fig. 1). (a) Density ($n/n_c$) of RPA protons, (b) longitudinal phase space ($x - P_x$) of RPA protons, (c) energy spectrum of protons crossing over the gold foil.

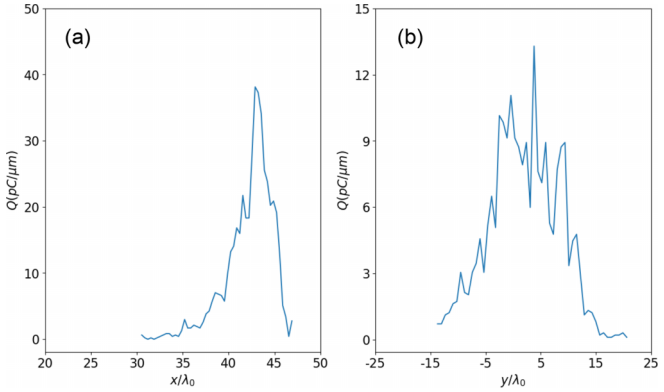


FIG. 4. (a) Longitudinal and (b) transverse profile of the accelerated proton beam shown in Fig. 3. The corresponding standard deviations are $\sigma_x = 3.82\lambda_0$ and $\sigma_y = 6.14\lambda_0$, respectively.

increased energy spread of around 40% in the case of aluminum with $Z = 10$ is mainly due to the low-energy plateau in the proton energy spectrum, as can be seen from the black line plot in Fig. 2(d). A similar plateau is also observed in the case of copper with $Z = 10$, which explains its relatively higher energy spread.

In order to understand the physics of the improved accelerated proton beam, we specifically look into the case of gold with $Z = 10$, which corresponds to Fig. 2(k). This case also corresponds to the lowest-energy spread among all the cases described in Table I. The results are summarized in Figs. 3(a) and 3(c) that show the number density ($n/n_c$) and longitudinal phase space ($x - P_x$) of the RPA protons, respectively. The normalized electrostatic potential ($\int E_x dx$) is shown in Fig. 3(b). Note that in Fig. 3(a), the number density of only RPA protons is plotted, although there is a NCD layer between $10\lambda_0$ and $20\lambda_0$. We observe a strong electrostatic potential around the gold foil (red line) in Fig. 3(b). This potential is formed by a TNSA-like mechanism [5] when the fast electrons, from the laser-RPA target interaction, cross the gold foil. The reflection of low-energy RPA protons from the gold foil due to the electrostatic potential can be seen from the phase-space plot in Fig. 3(c). The potential well around the gold foil is asymmetric due to the presence of NCD plasma on one side. Due to this, the higher-energy protons which can climb the uphill potential get an extra-energy boost after crossing the gold foil. Acceleration of protons in this region ($20 < x < 30\lambda_0$) can be seen from the phase-space plot. The presence of a middle NCD layer increases the length over which RPA acceleration is carried out by supplying the return current electrons for compensating the loss of fast electrons from the RPA target. This physics was discussed in detail in our earlier work [15].

The longitudinal and transverse profile of the accelerated proton beam is shown in Fig. 4. The corresponding standard deviations are $\sigma_x = 3.8\lambda_0$ and $\sigma_y = 6.1\lambda_0$, respectively. The total charge per unit length in the beam is found to be approximately 154.1 pC/μm. Assuming $\sigma_z = \sigma_y$, one can estimate the total charge to be approximately 0.8 nC, which corresponds to about $5 \times 10^9$ protons per laser pulse. Similarly, we estimate the duration of an accelerated proton beam ($\sigma_t$) by dividing $\sigma_x$ by the mean proton beam velocity ($\simeq 0.6c$). This gives a proton bunch duration of approximately 16 fs. Note that this corresponds to a beam current of around 50 kA with a power of ∼10 TW. The typical efficiency, from the laser to the proton beam, in all cases is found to be around 1–3%.

In order to demonstrate the role of metallic foil on energy filtering, we carried out simulations with only the RPA target and the gold foil, i.e., without the middle NCD layer. The simulations are carried out for three different charge states ($Z$) of gold foil, viz., $Z = 3$, 5, and 10. The choice of gold is motivated by the fact that the gold ions are practically immobile over the proton passage timescale due to their low charge to mass ratio ($Z/M$). For reference, simulations with pure RPA and RPA+NCD targets are also performed. The results are summarized in Fig. 5, where the top (T) and bottom (L) panels show the number density (normalized by $n_c$) and longitudinal phase space of RPA protons, respectively. The middle panel (M) shows the normalized electrostatic potential. The subplots T-1, M-1, and L-1 correspond to a case when the laser interacts with a stand-alone RPA foil, initially present at $10\lambda_0$. This represents a typical situation in the radiation pressure acceleration, where we observe the expansion of plasma due to the heating of electrons in the laser transparency phase [16]. Although protons are efficiently accelerated during this phase by transfer of energy to electrons, the accelerated proton beam has much larger energy spread, as can be seen from the phase-space plot (L-1). This is one of the critical limitations of the radiation pressure acceleration scheme. In contrast, the second vertical panel (T-2, M-2, L-2) represents the case with the RPA+NCD target, i.e., without the gold foil. In this case, we can see the increase in the maximum proton energy (from phase-space plots), indicating the efficient transfer of laser energy to the proton momentum through the RPA mechanism. Note that no sheath potential is observed in both of these reference simulations. This can be confirmed by comparing the RPA proton spectra and line-outs of electrostatic potential (blue vs red) shown in Fig. 6.

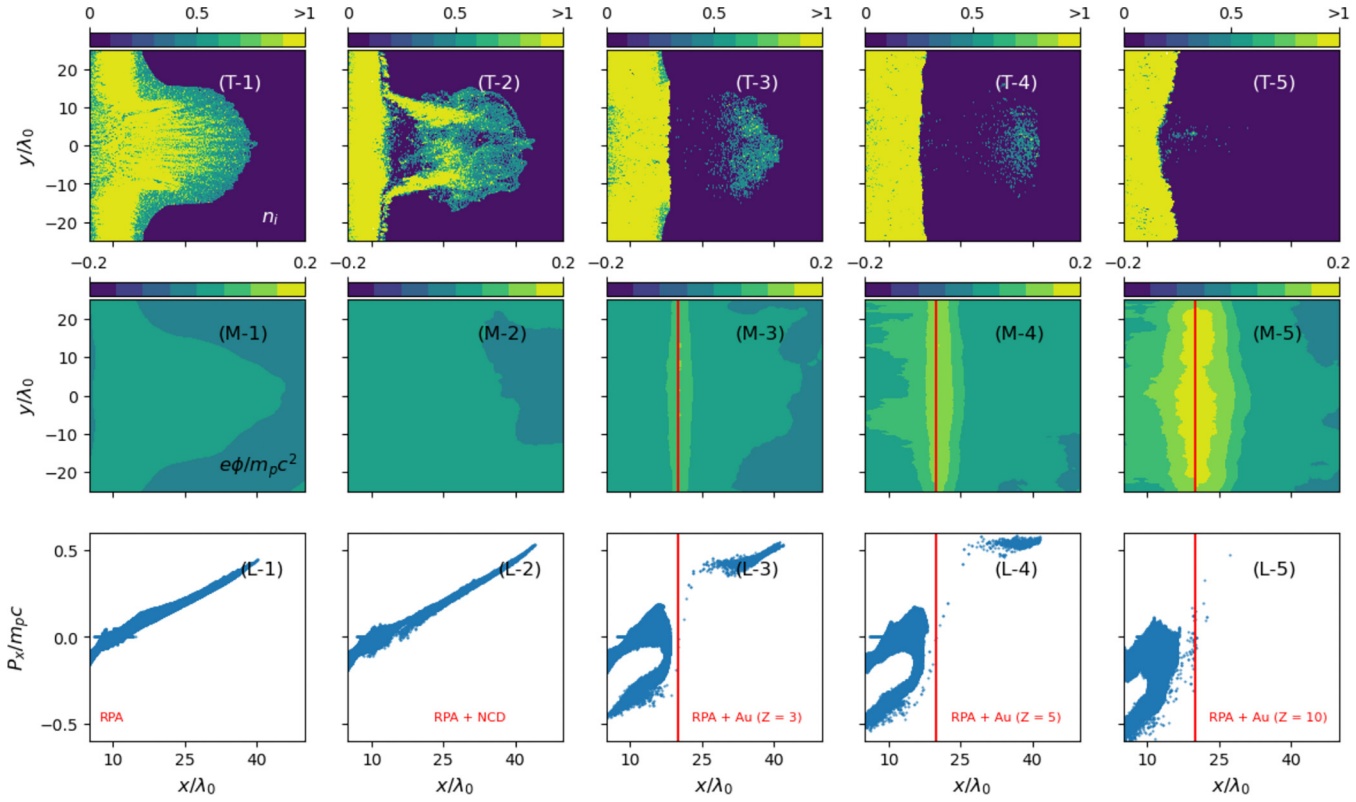


FIG. 5. Influence of gold foil, placed at the back of the RPA foil, on proton acceleration: A gold foil (red line) is placed at $X = 20\lambda_0$ and the initial location of the RPA foil is at $X = 10\lambda_0$. The normalized number density (top panels) and longitudinal phase space (bottom panels) are plotted at $\omega_0 t = 742$. The middle panels show the normalized electrostatic potential. With increasing the charge state ($Z$) of the gold foil, the reflection of protons near the location of the gold foil is observed. Quasimonoenergetic proton beam, crossing the gold foil, is observed for $Z = 3, 5$ whereas near-complete reflection of protons is seen for $Z = 10$.

In the presence of gold foil, placed $10\lambda_0$ behind the RPA foil, significant changes in the acceleration process are observed. The location of gold foil is shown with a red line.

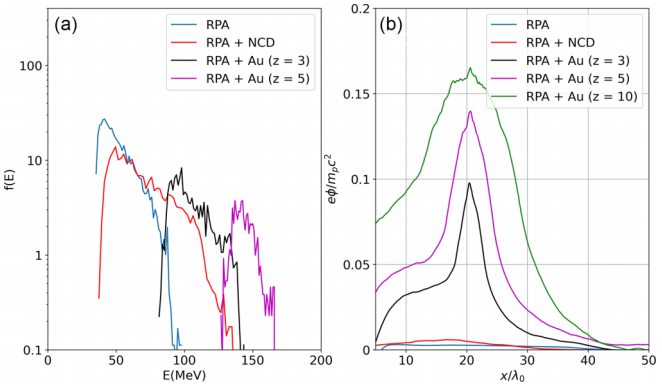


FIG. 6. (a) Improvement in energy spread of forwardly accelerated protons in the presence of gold foils with $Z = 3, 5$. In the absence of gold foil, a continuous spectrum (blue) is observed compared to a quasimonoenergetic beam with $Z = 3$ (black) and 5 (purple). The red plot shows the corresponding spectrum when a RPA+NCD target (i.e., no gold foil) is used. (b) The presence of sheath potential around gold foil for different charge states ($Z$). The barrier potential filters the low-energy RPA protons, resulting in an improved energy spectrum. For a $Z = 10$ charge state, the potential barrier reflects all the accelerated RPA protons.

With the introduction of gold foil, we observe the reflection of radiation pressure accelerated protons in the phase-space plots due to the electrostatic potential well. Indeed, when expanding plasma from the RPA target comes in contact with the gold foil, an electrostatic sheath is formed around the latter. The electrostatic field around the gold foil increases with increasing $Z$. A narrow proton beam having significantly less energy spread is seen to be crossing the gold foil with $Z = 3, 5$. With increasing $Z$, the number of protons crossing the gold foil reduces in such a way that practically very few protons are able to cross the foils with $Z = 10$ and beyond. The improvement in the energy spectrum of the forward accelerated protons can be seen in Fig. 6. The electric potential (normalized by the rest mass energy of the proton) associated with this sheath is also shown in Fig. 6(b). The potential is calculated by integrating the longitudinal electric field ($E_x$) along $y = 0$ with zero reference potential at the right boundary of the simulation box. With increasing the charge state of the gold foil, we observe that the maximum value of the potential also increases. Therefore, the incoming protons from the RPA target have to overcome this potential well. This explains the reflection of lower-energy protons. In addition, protons having sufficient energy to overcome the potential barrier get further accelerated while getting down the potential hill. This results in an increase in the mean energy of the accelerated beam from $Z = 3$ to $Z = 5$, as shown in the energy spectrum of accelerated protons in Fig. 6(a). On the contrary, the poten-

TABLE II. Charge and energy of accelerated protons with (case I) and without (case II) the near-critical-density (NCD) middle layer. The simulations are carried out by taking the charge states of the gold foil ($Z$) to be 3, 5, and 10.

| $Z$ of gold foil | $Q$ (pC/μm) Case I: NCD layer | $Q$ (pC/μm) Case II: No NCD layer | $E$ (MeV) Case I: NCD layer | $E$ (MeV) Case II: No NCD layer |
|---|---|---|---|---|
| 0 | 456.7 | 581.8 | 67.4 ± 19.8 | 51.2 ± 11.9 |
| 3 | 416.1 | 170.8 | 107.5 ± 17.7 | 104.2 ± 13.5 |
| 5 | 214.1 | 57.6 | 154.2 ± 19.4 | 143.6 ± 7.9 |
| 10 | 154.1 | | 224.0 ± 17.8 | |

tial well becomes so large that practically all the proton are reflected in the case of gold foil with $Z = 10$. Here, we would like to emphasize that due to the energy filtering at the gold sheath, the improved proton spectrum is obtained even with a linearly polarized laser.

Compared to the no-gold backfoil case (blue line in Fig. 6), significant improvement in the energy spectrum is observed when gold foil with $Z = 3, 5$ is placed behind the RPA foil. The energy of the accelerated proton beam for $Z = 3$ and $Z = 5$ was found to be $104.2 \pm 13.5$ and $143.6 \pm 7.9$ MeV, respectively. The corresponding charges are 170.8 and 57.6 pC/μm. Thus, the improvement in energy for $Z = 5$ is accompanied by a drop in an accelerated charge. In Table II, we compare these parameters with simulations in the presence of a middle NCD layer. This table clearly demonstrates the importance of the middle layer in improving the efficiency of the accelerator. The presence of a middle NCD layer leads to a significant increase in the charge without disturbing the energy of the accelerated beam. For example, from Table II, we see that the accelerated charge in the case of gold foil with $Z = 3$ increases the charge from 170.8 to 416.1 pC/μm due to the presence of a middle NCD layer. On the other hand, the energy in both cases is nearly the same.

## IV. DISCUSSION

Although the physics of laser transparency is still debated, it is certain that the RPA target eventually becomes transparent to the laser through depletion in electron density by escaping fast electrons. When the laser is transmitted through the target, the momentum transfer from the laser to the target ceases. This causes the termination of radiation pressure-driven acceleration. In addition, the RPA target electrons get significantly heated during the phase of laser transmission. These heated electrons can drag protons to higher energies [16,17], but at the cost of significant degradation in the accelerated proton energy spectrum. The design of the target shown in Fig. 1 is motivated by these facts. The return current provided by the near-critical-density middle layer supplies the flow of cold electrons to the RPA target, which replace the escaping fast electrons. This results in a reduction of density depletion during the RPA process, leading to suppression of the laser transparency. In other words, the middle near-critical-density layer reduces the electron depletion by supplying the return current electrons to compensate for the loss of fast electrons from the RPA target. Our previous studies [15] have demonstrated the suppression of laser transparency and improvement in the quality of the accelerated proton spectrum when a near-critical-density target is placed behind the RPA target. Such targets (RPA + near-critical-density target) were also considered in the earlier simulation studies [18,19] at higher laser intensities ($a_0 \sim 100$). The importance of this NCD layer is evident from Table II, where we see a significant increase in the accelerated charge in the presence of a middle foil. This feature is more prominent for the gold foil, with $Z = 10$.

Simulations clearly demonstrate that the energy filtering of an accelerated proton beam is done by the electrostatic sheath around the metallic foil. The strength of the electric field inside this sheath naturally increases with the charge state ($Z$) of the metallic foil. The sheath around the ionized metallic foil consists of ions with charge $+Z$ at solid density surrounded by a diffused electron cloud. The charge-separation electric field (in the $x$ direction) inside the sheath points away from the initial location of the metallic foil, as ions are less mobile compared to electrons. Therefore, the RPA protons have to work against this electric field when they are approaching the metallic foil. On the other hand, once the protons cross the metal ions, they are moving in the direction of the electric field. This explains the energy filtering of low-energy protons and additional energy boost to the high-energy protons which are able to cross the metallic foil. This collectively leads to improvement in the proton energy spectrum.

The dependence of the metallic foil material (Al, Cu, Au) on the energy of the proton beam comes from the fact that the dynamic evolution of the sheath field depends upon the mobility of the ions. The electric field inside the sheath starts to decrease once the ions respond to it. Naturally, the RPA protons transporting through this sheath get affected by this electric field. Out of three chosen materials for the metallic foil, gold is the least mobile due to its lowest $Z/M$ ratio. For the timescale of passage of the protons, gold ions are practically immobile for $Z \leqslant 10$. Therefore, in the case of gold, with increasing $Z$ the sheath potential rises such that the maximum energy increases at the cost of accelerated charge. For aluminum and copper, the ion mobility increases with increasing $Z$. Therefore, the number of low-energy protons crossing the metal foil also increases. This explains the low-energy plateau in the spectrum for aluminum and copper, with $Z = 10$.

## V. SUMMARY AND CONCLUSION

In this work, we demonstrated the radiation pressure-driven proton acceleration by a linearly polarized laser with a significantly improved energy spread. Typically, for the RPA process, a linear polarized laser is considered to be "not so suitable" due to excess electron heating. This issue is addressed through a different target design where a partially ionized metallic foil ($Z \leqslant 10$) is placed behind the RPA foil. An electrostatic sheath is formed around the foil by the escaping fast electrons which are generated by the interaction of a linearly polarized laser with the RPA target. This sheath helps to improve the energy spread of the accelerated proton beam by reflecting the low-energy component of the spectrum. The presence of a near-critical-density middle layer improves the RPA process to increase the accelerated charge. By performing simulations with various materials for the metallic foil,

we propose that energy filtering with a different target is experimentally viable.

The method offers an attractive alternative to conventional passive magnetic systems [20] for the energy selection of RPA proton beams. Such systems have experimentally demonstrated energy selection and focusing of low-energy protons using either quadruple magnets [21,22] or pulsed solenoids [23,24] in laser-plasma experiments. These systems would require significantly higher magnetic fields (∼30–50 T) for the proton energies obtained in our work ($E_p \sim$ 200 MeV) as the required magnetic field strength scales as $B \propto \sqrt{E_p}$ [25]. Therefore, building a such passive magnetic system for a RPA-based compact accelerator is a major engineering challenge. On the other hand, the proposed method does*in situ* energy filtering. It should be noted that quasimonoenergetic proton beams by active systems involving laser engineering [26,27] and complex target design [28,29] have been reported earlier, but here we employed a combined RPA-TNSA mechanism in our method.

One of the limitations of this scheme is to control the charge state of the metal foil. With a higher charge state ($Z >$ 10), it is found that the sheath potential reflects all the accelerated protons. Although the charge state is not self-consistently evolved in the present work, it is hoped that the presence of a middle layer will play a crucial role in controlling it by avoiding direct interaction of the gold foil with an intense layer. This hypothesis can be tested either experimentally or through numerical simulations involving ionization physics. The latter approach will be adopted in future studies.

Simulations also demonstrate the possibility of laser-driven acceleration of protons to energies and fluxes which are relevant to hadron therapy. The laser parameters used in the simulations are well within the reach of present-day laser technology. Therefore, it is envisaged that a laser-plasma based accelerator will be able to provide a viable alternative for such a treatment in the near future.

## ACKNOWLEDGMENT

We wish to acknowledge the support for computational resources at the Homi-Bhabha National Institute (HBNI), Mumbai.

[1] A. Macchi, M. Borghesi, and M. Passoni, Rev. Mod. Phys. **85**, 751 (2013).
[2] R. R. Wilson *et al.*, Radiology **47**, 487 (1946).
[3] S. V. Bulanov, J. J. Wilkens, T. Z. Esirkepov, G. Korn, G. Kraft, S. D. Kraft, M. Molls, and V. S. Khoroshkov, Phys. Usp. **57**, 1149 (2014).
[4] K. W. Ledingham, P. R. Bolton, N. Shikazono, and C.-M. C. Ma, Appl. Sci. **4**, 402 (2014).
[5] S. Wilks, A. Langdon, T. Cowan, M. Roth, M. Singh, S. Hatchett, M. Key, D. Pennington, A. MacKinnon, and R. Snavely, Phys. Plasmas **8**, 542 (2001).
[6] T. Esirkepov, M. Borghesi, S. V. Bulanov, G. Mourou, and T. Tajima, Phys. Rev. Lett. **92**, 175003 (2004).
[7] A. Macchi, S. Veghini, and F. Pegoraro, Phys. Rev. Lett. **103**, 085003 (2009).
[8] F. Pegoraro and S. V. Bulanov, Phys. Rev. Lett. **99**, 065002 (2007).
[9] A. Sgattoni, S. Sinigardi, L. Fedeli, F. Pegoraro, and A. Macchi, Phys. Rev. E **91**, 013106 (2015).
[10] B. Eliasson, New J. Phys. **17**, 033026 (2015).
[11] Y. Wan, C. H. Pai, C. J. Zhang, F. Li, Y. P. Wu, J. F. Hua, W. Lu, Y. Q. Gu, L. O. Silva, C. Joshi, and W. B. Mori, Phys. Rev. Lett. **117**, 234801 (2016).
[12] B. S. Paradkar and S. Krishnagopal, Phys. Rev. E **93**, 023203 (2016).
[13] A. Robinson, M. Zepf, S. Kar, R. Evans, and C. Bellei, New J. Phys. **10**, 013021 (2008).
[14] B. Qiao, M. Zepf, M. Borghesi, and M. Geissler, Phys. Rev. Lett. **102**, 145002 (2009).
[15] B. S. Paradkar, Phys. Plasmas **28**, 030702 (2021).
[16] A. Henig, D. Kiefer, K. Markey, D. C. Gautier, K. A. Flippo, S. Letzring, R. P. Johnson, T. Shimada, L. Yin, B. J. Albright, K. J. Bowers, J. C. Fernandez, S. G. Rykovanov, H. C. Wu, M. Zepf, D. Jung, V. K. Liechtenstein, J. Schreiber, D. Habs, and B. M. Hegelich, Phys. Rev. Lett. **103**, 045002 (2009).
[17] L. Yin, B. Albright, B. Hegelich, K. J. Bowers, K. Flippo, T. Kwan, and J. Fernández, Phys. Plasmas **14**, 056706 (2007).
[18] S. S. Bulanov, E. Esarey, C. B. Schroeder, S. V. Bulanov, T. Z. Esirkepov, M. Kando, F. Pegoraro, and W. P. Leemans, Phys. Rev. Lett. **114**, 105003 (2015).
[19] Z. Zhang, X. He, Z. Sheng, and M. Yu, Phys. Plasmas **17**, 043110 (2010).
[20] S. Chen, M. Gauthier, D. Higginson, S. Dorard, F. Mangia, R. Riquier, S. Atzeni, J.-R. Marquès, and J. Fuchs, Rev. Sci. Instrum. **85**, 043504 (2014).
[21] S. Ter-Avetisyan, M. Schnürer, R. Polster, P. Nickles, and W. Sandner, Laser Part. Beams **26**, 637 (2008).
[22] M. Schollmeier, S. Becker, M. Geissel, K. A. Flippo, A. Blazevic, S. A. Gaillard, D. C. Gautier, F. Gruner, K. Harres, M. Kimmel, F. Nurnberg, P. Rambo, U. Schramm, J. Schreiber, J. Schutrumpf, J. Schwarz, N. A. Tahir, B. Atherton, D. Habs, B. M. Hegelich, and M. Roth, Phys. Rev. Lett. **101**, 055004 (2008).
[23] K. Harres, I. Alber, A. Tauschwitz, V. Bagnoud, H. Daido, M. Günther, F. Nürnberg, A. Otten, M. Schollmeier, J. Schütrumpf *et al.*, Phys. Plasmas **17**, 023107 (2010).
[24] T. Burris-Mog, K. Harres, F. Nürnberg, S. Busold, M. Bussmann, O. Deppert, G. Hoffmeister, M. Joost, M. Sobiella, A. Tauschwitz *et al.*, Phys. Rev. ST Accel. Beams **14**, 121301 (2011).
[25] I. Hofmann, Phys. Rev. ST Accel. Beams **16**, 041302 (2013).
[26] C. A. J. Palmer, N. P. Dover, I. Pogorelsky, M. Babzien, G. I. Dudnikova, M. Ispiriyan, M. N. Polyanskiy, J. Schreiber, P. Shkolnikov, V. Yakimenko, and Z. Najmudin, Phys. Rev. Lett. **106**, 014801 (2011).
[27] D. Haberberger, S. Tochitsky, F. Fiuza, C. Gong, R. A. Fonseca, L. O. Silva, W. B. Mori, and C. Joshi, Nat. Phys. **8**, 95 (2012).
[28] B. M. Hegelich, B. Albright, J. Cobble, K. Flippo, S. Letzring, M. Paffett, H. Ruhl, J. Schreiber, R. Schulze, and J. Fernández, Nature (London) **439**, 441 (2006).
[29] C.-K. Huang, B. Albright, L. Yin, H.-C. Wu, K. Bowers, B. Hegelich, and J. Fernández, Phys. Plasmas **18**, 056707 (2011).